

Toward a Framework for Adaptive Impedance Control of an Upper-limb Prosthesis

Laura Ferrante

School of Computer Science,
University of Birmingham,
Birmingham, UK
lxf656@student.bham.ac.uk

Mohan Sridharan

School of Computer Science,
University of Birmingham,
Birmingham, UK
M.Sridharan@bham.ac.uk

Claudio Zito

Autonomous Robotics Research Centre,
Technology Innovation Institute,
Abu Dhabi, UAE
Claudio.Zito@tii.ae

Dario Farina

Department of Bioengineering
Imperial College London,
London, UK
D.Farina@imperial.ac.uk

Abstract: This paper describes a novel framework for a human-machine interface that can be used to control an upper-limb prosthesis. The objective is to estimate the human’s motor intent from noisy surface electromyography signals and to execute the motor intent on the prosthesis (i.e., the robot) even in the presence of previously unseen perturbations. The framework includes muscle-tendon models for each degree of freedom, a method for learning the parameter values of models used to estimate the user’s motor intent, and a variable impedance controller that uses the stiffness and damping values obtained from the muscle models to adapt the prosthesis’ motion trajectory and dynamics. We experimentally evaluate our framework in the context of able-bodied humans using a simulated version of the human-machine interface to perform reaching tasks that primarily actuate one degree of freedom in the wrist, and consider external perturbations in the form of a uniform force field that pushes the wrist away from the target. We demonstrate that our framework provides the desired adaptive performance, and substantially improves performance in comparison with a data-driven baseline.

Keywords: Myocontrol, muscle-tendon models, online impedance adaptation, human motor intent, upper-limb prosthesis

1 Introduction

Consider the simple task of carrying a cup of coffee. Forces arise from the physical interaction between the liquid, the cup, and the human hand. To perform this task, humans typically modulate the limb impedance (i.e., stiffness, damping, inertia) by co-activation of agonist and antagonist muscles, in order to make the physical interaction with the environment (i.e. the cup of coffee, plus unexpected perturbations) stable. Modulation of the impedance properties of the robot (i.e., the prosthesis) is thus a crucial aspect in prosthesis control given that the user with prosthetic limbs physically interacts with the environment. However, none of the commercially available upper-limb prostheses allow simultaneous control of the kinematic and dynamic properties of the prosthesis. This is due to the challenges in decoding the human motor intent from low bandwidth surface electromyography (sEMG) signals [1], and the high redundancy of human motor control. In fact, there is a non-unique mapping from sEMG signals to target joint kinematics since the same action can be performed at different levels of muscles contraction (i.e., impedance).

Data-driven methods are the state of the art in prosthesis control of commercially available devices [2, 3]. These methods map sEMG signals to control commands (i.e., kinematics) in an offline training phase. Although effective for simple movement in controlled experimental settings, these methods do not explicitly represent or use information about the human joint impedance in the con-

trollers. As a result, performance deteriorates in practical settings where factors such as the physical interactions with the environment cause the sEMG features to change drastically from those observed during training, requiring the user to continuously adapt the muscle contractions (EMG signals) to control the prosthesis. Moreover, the representation of human motion intent only in terms of kinematics makes it difficult for designers and users to understand the prosthesis' operation.

Existing methods that seek to provide simultaneous control of joint position and joint stiffness use muscle-tendon models to decode human motor intent [4, 5, 6, 7, 8]. The stiffness extracted from the muscle-tendon models is typically tuned directly to satisfy the controller's stability constraints, which can lead to a mismatch between the dynamics of the muscle-tendon model and those of the robot's motion. The transparency and controllability achieved by these methods are thus rather limited.

The main contribution of this paper is a framework for an sEMG-driven Human Machine Interface (HMI) that provides the user with three Degrees of Control (DoC), i.e., the control of joint position, stiffness, and damping, per Degree of Freedom (DoF) of an upper-limb prosthesis. Our framework comprises two blocks in cascade—see Figure 1(A). The first block incorporates muscle-tendon models and maps the sEMG signals to an estimate of the user's motor intent in terms of kinematics (i.e., joint position) and dynamics (i.e., joint stiffness and joint damping). The second block then executes this motor intent through a robot system based on a variable position-based impedance controller, allowing online position control and adaptation of the prosthesis' impedance.

Our framework's design is motivated by two desiderata. First, to ensure that the *intended dynamics* given by the first block matches the prosthesis' dynamics, the stiffness and damping estimated from the muscle-tendon models are used in the variable impedance controller; it also enhances the framework's *transparency*. Second, the values of the muscle-tendon models' parameters need to be set suitably in order to converge to a representation of the intended dynamics that enables robust adaptation of the robot's dynamics. In our framework, the prosthetic device's joint position trajectory is used as an optimization signal in an offline training phase to set the muscle-tendon parameter values such that the resulting joint stiffness and damping enable robust tracking of the intended joint position and adaptation of the joint impedance during online operation.

To fully explore the interplay between the framework's components, we conducted a study with able-bodied participants focusing primarily on the flexion-extension of the wrist to control a single DoF of a simulated robot. We evaluated the framework during online reaching tasks and investigated whether the user could counter perturbations in the form of force fields that push the simulated wrist away from a target, making impedance adaptation necessary to maintain stability and complete the task. Experimental results demonstrate that our framework's performance is comparable to a state-of-the-art data-driven baseline in the absence of perturbations and substantially better in the presence of perturbations. Overall, our study provides a deeper understanding of the estimation and mapping of user motor intent to the control of an upper-limb prosthesis, which could aid in the mapping of user intent to robot control in other applications.

2 Related work

There is well-established literature on human-motor control and the importance of muscle impedance adaptation for stable physical interaction with the environment [9, 10, 11]. Impedance control is a widely used paradigm to define the mechanical impedance of the robot at the point of contact with the object being manipulated [12]. However, implementing variable impedance behaviour on a robot is challenging since the choice of controller gains depends on the task, system constraints, and environmental properties. In human-robot interaction scenarios that require the robot to physically cooperate with humans or acquire the user's control skills (e.g., teleoperation, prosthesis control), it is crucial to allow the user to control the robot's kinematics and physical interaction with the environment. This requirement is more pronounced in prostheses control because the user and the robot (prosthesis) are two agents of the same system.

Surface electromyography (sEMG) signals are used widely to establish the physical interaction between the user and the prosthesis because they are non-invasive and easy to use. Most existing methods that attempt to implement an EMG-based HMI for simultaneous control of joint position and impedance of a single DoF, estimate stiffness directly from the magnitude of the EMG signals, even when muscle-tendon models are used within the pipeline and the impedance parameters could

be retrieved from the muscle-tendon state [4, 5, 6, 7, 8]. In addition, joint damping is often not computed from the EMG signals or the muscle-tendon models’ state in these methods; it is instead set as a function of the stiffness. This means that the dynamics of the muscle-tendon model does not match that of the robot, possibly leading to unwanted behaviour and instability. Other methods first estimate the stiffness and damping from the measured torque and then learn a model (e.g., a polynomial function of the EMGs) of the stiffness and damping [13, 14]. We argue that these approaches make simplifying assumptions on the relationship between the amplitude of the EMGs and the torque; since they rely on the relationship between EMG signals, the output torque and stiffness are very sensitive to the amplitude and shape of the EMG signals. No commercial upper-limb prosthesis used for daily life tasks allows adaptation of joint impedance properties due to limitations imposed by the hardware design and the challenges in implementing the desired adaptive behaviour.

Researchers have explored different function approximators for simultaneous and proportional myocontrol over one or more DoFs of upper-limb prostheses [2, 15, 16]. Unsupervised methods, which rely on Non-Negative Matrix Factorization (NNMF) to extract command signals from EMGs, have been used to provide simultaneous control and robustness to issues such as electrode shifting that induce EMG signal deterioration [17]. Results indicate that non-linear regression outperforms linear regression during the training phase, but results are comparable on unseen testing data [18]. In recent years, deep learning methods are increasingly being used to improve feature extraction and learn complex non-linear mapping between EMGs and target motion trajectories or classes [19, 20]. While these data-driven methods allow simultaneous and proportional control of two DoFs, they do not explicitly learn the human motor intent in terms of joint stiffness and damping, and do not allow the user to adapt the prosthesis’ impedance in the presence of previously unseen environmental perturbations. Moreover, there is lack of evaluation of these methods in scenarios where impedance adaptation is required to maintain system stability.

3 Problem Formulation and Framework

Figure 1-A provides an overview of our framework in the context of controlling a single DoF: flexion and extension at the wrist. The first block of the framework, i.e., *Detection of Human Motor Intent*, takes as input the sEMG signals from the user’s wrist flexor and extensor muscles (ch_1, ch_2) and estimates the user’s motor intent in terms of reference kinematics $s_r = (q_r, \dot{q}_r, \ddot{q}_r)$, and joint stiffness K and damping D. This estimation is done in two phases. In *phase 1*, the sEMG signals drive the lumped muscle-tendon units (MTU_1, MTU_2) that generate the muscle-tendon forces (F_1, F_2) based on the muscle-tendon contraction dynamics; the muscle-tendon stiffness and damping are computed from the state of the MTUs. The muscle-tendon variables are then mapped to the joint space of the robot model to obtain joint torque τ_r , stiffness K, and damping D. In *phase 2*, τ_r is applied to the simulated robot model to actuate the robot’s joint q_r and obtain the human intended joint kinematics s_r . The framework’s second block, i.e., *Prosthesis control*, executes the motor intent obtained from the previous block on the robot plant using a position-based variable impedance controller that tracks s_r based on K and D. The robot’s state q_f is the framework’s output and the user’s visual feedback. If an external perturbation acts on the robot plant, the user can use this feedback to modulate the plant’s impedance and reduce the error between s_r and the plant’s state.

In this paper, we implement our framework and the associated HMI in the CoppeliaSim simulation environment. We use the *Puma 560* robot manipulator as the robot arm because its characteristics are well-understood; we only consider the chain from link 0 to link 2 of this robot and control joint 2 with our framework. In practice, since we consider a single DoF, any simple 1-DoF robot can be used. Note that when the framework is used with a real prosthesis, the *simulated robot model* in Figure 1-A will be a simulation of the prosthesis and the *robot plant* will be the real prosthesis.

Below, we describe our framework’s components in detail (Section 3.1, Section 3.2). We also describe the optimization method used to estimate the values of the muscle-tendon models’ parameters values (Section 3.3), highlighting the difficulties in identifying parameter values that result in stiffness and damping values suitable for adapting the gains of the position-based variable impedance controller. The time dependence of each variable is dropped in the notation for simplicity.

3.1 Detection of human motor intent

As stated earlier, the first block of our framework maps the input sEMG signals from the user to an estimate of the user’s motor intent based on the muscle-tendon models.

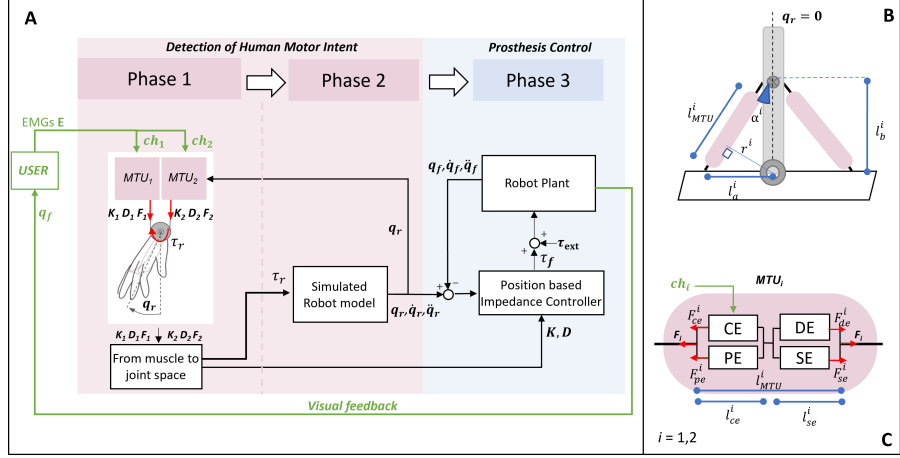


Figure 1: (A) High-level block diagram of our framework to control a 1 DoF robot arm. The framework comprises a *Detection of Human Motor Intent* block and a *Prosthesis Control* block. The first block maps sEMG signals from the user’s wrist muscles (ch_1, ch_2) to estimates of the user’s motor intent in terms of kinematics, i.e., $s_r = (q_r, \dot{q}_r, \ddot{q}_r)$ and dynamics, i.e., joint stiffness and damping (K, D). The second block executes the motor intent on the robot plant, using a variable impedance controller to track s_r based on K and D . The framework’s output q_f is also the visual feedback that can be used by the user to module impedance in response to external perturbation on the robot plant. (B) Arrangement of muscle-tendon units on the link of the simulated robot model. (C) Diagram of the forces generated by the elements within each muscle-tendon unit. MTU_i comprises muscle (CE, PE) and tendon components (DE, SEE) of length l_{ce}^i and l_{se}^i respectively.

Muscle-tendon models The biomechanical model of each MTU_i is based on the well established Hill’s phenomenological muscle-tendon model [21]. Each MTU_i (of length l_{MTU}^i) is composed of a muscle (of length l_{ce}^i) in series to a tendon (of length l_{se}^i). The muscle is modeled by a contractile element (CE) and a parallel elastic element (PE). The tendon is made up of a serial elastic element (SE) in parallel to a damper element (DE). The system at equilibrium is described by:

$$F_{ce}^i(l_{ce}^i, l_{ce}^i, ch_i) + F_{pe}(l_{ce}^i) = F_{se}^i(l_{ce}^i, l_{MTU}^i) + F_{de}(l_{ce}^i, l_{ce}^i, l_{MTU}^i, ch_i) \quad (1)$$

where the EMG signal ch_i is normalised in the range $(0, 1]$ with respect to the maximum value generated by the subject during the training phase. For detailed information about the numerical simulation of the muscle-tendon contraction dynamics, and activation dynamics, please see [22, 23].

Geometric arrangement of MTUs on robot Figure 1-B provides an overview of the arrangement of the MTUs on the simulated robot model. Each MTU_i is virtually attached to the link from the Center of Mass (CoM) of the link (l_a^i) to a fixed base (l_b^i), i.e., the length of l_{MTU}^i varies as a function of q_r . Given α_i and the initial joint position $q_r = 0$, we can compute l_b^i as $l_{MTU}^i \sin \alpha_i$. l_a^i and l_b^i are kept constant during the simulation and control, while $l_{MTU}^i(q_r)$ and the moment arm $r^i(q_r)$ vary as a function of q_r :

$$l_{MTU}^i = \sqrt{(l_a^i)^2 + (l_b^i)^2 - 2l_a^i l_b^i \cos(\pi/2 - q_r)} \quad (2)$$

where the muscle-tendon contraction velocity \dot{l}_{MTU}^i is computed by numerical differentiation. To transform the muscle-tendon forces, stiffness, and damping to the joint space, we define the Jacobian matrix $\mathbf{R} = [r^1 \ r^2] = [\frac{\partial l_{MTU}^1(q_r)}{\partial q_r} \ \frac{\partial l_{MTU}^2(q_r)}{\partial q_r}]^T$ containing the moment arms r^i of the two MTUs:

$$r^i(q_r) = \frac{\partial l_{MTU}^i(q_r)}{\partial q_r} = l_b^i \sin \alpha^i(q_r) \quad \text{with} \quad \alpha^i(q_r) = \arccos\left(\frac{-(l_a^i)^2 + (l_b^i)^2 + (l_{MTU}^i)^2}{2l_a^i l_b^i}\right) \quad (3)$$

Joint stiffness and damping estimation The stiffness and damping of each MTU are first estimated from the muscle-tendon state and then mapped to the joint space. K_i is modeled as the muscle fiber stiffness K_m^i in series with the tendon’s stiffness K_t^i , i.e., $K_i = K_m^i K_t^i / (K_m^i + K_t^i)$. K_m^i is computed as the directional derivative of $F_{ce}(l_{ce}^i, l_{ce}^i, ch_i)$ with respect to unit vector of l_{ce}^i [24]:

$$K_m^i = \frac{\partial F_{ce}^i(l_{ce}^i, l_{ce}^i, ch_i)}{\partial l_{ce}^i} \quad (4)$$

Similarly, K_t^i is computed as the directional derivative of $F_t^i = F_{se}^i + F_{de}^i$ with respect to unit vector of $l_{se}^i = l_{MTC}^i - l_{ce}^i$. Muscle and tendon damping (D_m^i, D_t^i) are computed as directional derivatives with respect to muscle contraction velocity \dot{l}_{ce}^i and tendon extension velocity $\dot{l}_{se}^i = \dot{l}_{MTU}^i - \dot{l}_{ce}^i$.

Mapping from muscle space to joint space Forces generated by MTU_i result in the net torque $\tau_r = [F_1, F_2]^T \mathbf{R}$. We compute the joint space stiffness considering also the contribution given by the varying moment arms as a function of q_r , according to the following definition of stiffness [25]:

$$K = \frac{\partial \tau_r}{\partial q_r} = \frac{\partial \mathbf{R}^T}{\partial q} [F_1, F_2]^T + \mathbf{R}^T \text{diag}([K_1, K_2]) \mathbf{R} \quad (5)$$

The joint damping is computed as $D = \sum_{i=1}^2 (D_i(r^i)^2)$.

3.2 Prosthesis Control

Human motor intent at time t is represented by the joint torque $\tau_r(t)$, stiffness $K(t)$, and damping $D(t)$, estimated as described above. As stated earlier, our framework's second block executes this intent on the robot plant using a variable impedance controller. Recall also that when a physical prosthesis is used, it will be the robot plant.

Variable impedance control First, the torque output of MTUs ($\tau_r(t)$) is applied to the robot's joint using the forward dynamics model, to obtain the joint state $s_r(t) = (q_r(t), \dot{q}_r(t), \ddot{q}_r(t))$. A position-based variable impedance controller is used to track $s_r(t)$ by adapting $K(t)$ and $D(t)$. Consider the generic dynamic model for a robot with a single rotational joint:

$$M\ddot{q}_r(t) + g(q_r(t)) = \tau_f(t) + \tau_{ext}(t) \quad (6)$$

where M is the link's joint space inertia, g is the gravity compensation torque, and $\tau_{ext}(t)$ is the external perturbation acting on the robot joint. Building on the impedance control paradigm without force-torque sensor readings [12], we define the control law as:

$$\tau_f = M\ddot{q}_r(t) + K(q_r(t) - q_f(t)) + D(\dot{q}_r(t) - \dot{q}_f(t)) + g(q_r(t)) \quad (7)$$

Any external perturbation (τ_{ext}), e.g., a force field acting on the joint and preventing it from reaching a target position, affects the state of the robot plant only, while the state of the simulated robot model and the MTUs states represent the user motor intent based on the input sEMG signal only. In the absence of external perturbations ($\tau_{ext} = 0$), q_r matches q_f . If τ_{ext} is not zero, depending on K and D , q_f will start diverging from q_r . The observed robot pose q_f serves as visual feedback for the user, who can compensate for the perturbation through online modulation of the muscles contraction and adaptation of the simulated robot's state and gains (K, D).

3.3 Learning parameter values and transparency

For the two blocks of the framework to work as described above, it is important to set suitable values for the parameters of the MTUs. Identifying such values for the parameters of MTUs is challenging since the underlying optimization process usually minimizes the root mean square error between a reference torque and the torque predicted by the MTUs without any prior knowledge of the interaction between elements within the MTU. The problem is ill-posed even with upper and lower bounds on the values of parameters since multiple combinations of parameters can generate the same net joint torque (τ_{ref}) and thus the same reference joint position, q_r , but most of these combinations may provide gains (K, D) that do not match the user-desired dynamic behaviour, resulting in an unstable impedance controller and a q_f that is significantly different from the corresponding q_r . This is a *critical issue that undermines model transparency, making it difficult to fully understand the dynamics of contraction and to extract valid gain values*.

In our architecture, we attempt to address the critical parameter estimation problem by:

- making structural assumptions regarding the MTU;
- reducing the number of parameters to be estimated to maximize their inter-dependency (See Section A.2); and

- defining an optimization framework that includes the position-based impedance controller and uses q_f as optimization signal.

The choice of the muscle-tendon parameters influences the interaction between the individual elements in the muscle and in the tendon, which (in turn) affects the muscle and tendon stiffness and damping. We found experimentally in initial sensitivity studies that the result of the optimization is highly sensitive to the relative lengths of the muscle and the tendon. Hence, we defined the muscle-tendon model structure to have a long tendon compared with the muscle. This is based on existing literature which indicates that such a muscle-tendon system enhances control and impedance modulation [26, 27]. In addition, the preliminary sensitivity studies indicated that some parameters did not make any substantial contribution to the offline tracking performance. Based on this observation, we made two simplifications to the MTU parameters to be estimated: (i) the pennation angle, i.e., the angle between the muscle and the tendon, is set to be constant at zero; and (ii) l_{opt}^i is learned directly from data instead of using a more complex closed-form equation used in prior work [28, 6]. Finally, instead of using the torque τ_r as the optimisation signal, we used the final joint position q_f that depends on the interaction dynamics defined by the gains (K, D). This change in the optimisation signal enabled us to incorporate the stiffness and damping estimated from the muscle-tendon models' state in the position-based variable impedance controller.

We formally define the prediction function that acts on the input $ch_1(t), ch_2(t)$ to produce the final joint position $q_f(t)$ based on the parameters of the MTUs $\bar{\mathbf{p}}$ as:

$$q_f(t) = f([ch_1(t), ch_2(t)]; \bar{\mathbf{p}}) \quad (8)$$

The optimization problem is then defined as:

$$\min_{\bar{\mathbf{p}}} \sqrt{\frac{\sum_{t=1}^T (f([ch_1(t), ch_2(t)]; \bar{\mathbf{p}}) - q_f^{train}(t))^2}{T}} \quad (9)$$

with the parameter values explored through simulated annealing. Here, q_f^{train} is the measured wrist flexion-extension angular position. Only the subset $\bar{\mathbf{p}}$ of parameters \mathbf{p} defining the MTUs (per DoF) is considered during training. In particular, the slack length of the tendon is set to 2/3 of l_{MTU}^i so that the muscle-tendon complex has a long tendon and short muscle, and the constraint that limits the maximum extension of the tendon (l_{se}^i) is set to 10% of l_{se}^i [26]. The lower and upper bounds of $\bar{\mathbf{p}}$ are set experimentally or based on prior work [29] (See Section A.2);

Notice that we neither measure the human joint impedance nor claim to learn a stiffness and damping that mimics the biological one. Instead, we design the framework and define the optimization of the MTUs' parameters values, as explained above, to provide the user with a coherent representation of the dynamics of the MTUs and the robot, in an attempt to enhance the controllability provided to the user. Section 4 describes the protocol for acquiring training data.

4 Experimental Evaluation

In this section, we describe the experimental setup and results of the experimental evaluation.

4.1 Experimental Setup

Eight able-bodied, right-handed volunteers (five females, three males, age: 27.87 ± 3.64) without neuromuscular disorders or prior experience in myocontrol, took part in the study approved by our university's ethics committee. In each trial, the subject sat in front of a screen, with the arm along the side of the body in a neutral resting position. The subject wore a Myoband by ThalmicLab (eight sEMG channels, frequency 200 Hz) in the upper forearm to record the muscle activations ($\mathbf{E}(t)$) as they performed a reaching task; We consider channel 4 and channel 8 of the device as EMG signals of the main extensor and flexor muscle (ch_1, ch_2). The wrist position q_f^{train} was tracked with a Qualysis motion capture system. The raw EMGs were bandpass-filtered (20 - 500 Hz) and full-wave rectified before the root-mean-square (RMS) temporal features were extracted (moving window of length 160ms and step size 40 ms).

Training phase Figure 2A-B provides an overview of data acquisition to train muscle-tendon models. The subject viewed a screen with a Cartesian space whose axes were wrist joint positions (in *Degrees*) for ulnar-radial deviation and flexion-extension respectively. During each trial, a visual cue

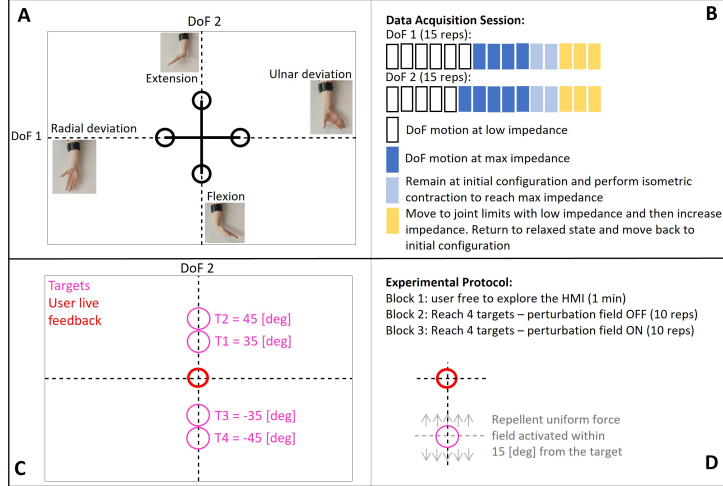


Figure 2: **A-B)** Data acquisition: subject’s wrist motions are guided by the black visual cue shown in A) with experimental protocol shown in B). **C-D)** Reaching task: subject receives visual feedback of the predicted position of their hand (red circle in C)) and has to reach targets T1-T4; experimental protocol and perturbation field are shown in D).

moved along one of the axes and the subject had to move their wrist to match this cue, modulating their muscle impedance properties as needed. Notice that even when we are primarily activating a single DoF (e.g. flexion extension), there is some “unintentional” motion along the other DoF (e.g. ulnar-radial deviation). For this reason, despite focusing on the control of a single DoF (flexion-extension), we asked the subject (in the data collection phase) to perform also 15 repetitions of ulnar-radial deviation, so that we can observe the flexion-extension motion. Data (i.e., EMG signals, wrist position q_{gt}) from 15 trials of each kind of motion (total of 30 trials) were collected. A 60 – 40 split of this data was used for training and validating the muscle models, with optimization based on Simulated Annealing (500 iterations, 5000 function evaluations, initial value of temperature 300, annealing interval 50) [30].

Online evaluation We report results corresponding to flexion-extension movements during online evaluation although the target movements involve the co-contraction of other muscles as well. In each trial, a human subject was asked to reach a target position displayed on the monitor (purple circle) as accurately and quickly as possible. Once at the target, the subject had to maintain the position for three seconds. The radius of the circle indicating the target and the actual position of the simulated wrist was eight and six density-independent pixels (respectively), requiring the subject to be precise. The subject received visual feedback of the predicted position of their wrist (Figure 2C). The experimental trials for each subject had three sessions (Figure 2D). In the third session, the subject experienced a force field that pushed the simulated wrist away from the target; stiffness and damping had to be adapted to complete the task. The subject was told that some force would perturb the simulated robot, but no information about the force field (type, magnitude, location in workspace) was provided. The magnitude of the perturbation was defined as a percentage of the maximum torque that can be generated by the subject; its average magnitude is 20Nm.

Data-driven baseline and hypotheses The baseline was a neural network described in prior work that learned a mapping from EMG features to the reference kinematics [3]. The training data was the same for our framework and the baseline and we trained the model to match the performance reported in [3]. To ensure a fair comparison, a PD controller was added in cascade to track the joint position predicted by the baseline q_r . This controller had constant high stiffness ($K_B = 100N/rad$) to support accurate motion tracking and perturbation rejection. The damping gain was computed assuming a critically damped system: $D_B = \sqrt{K_B/4Ns}/rad$ [31]. For the baseline, q_f indicates the output position when tracking q_r with K_B and D_B . The choice of this baseline is motivated by the fact that existing methods that include muscle-tendon models do not use the stiffness directly computed from the muscle-tendon states, but the joint stiffness is usually tuned to achieve stability and position tracking during an offline training phase. This is in principle equivalent to our chosen baseline that uses a high-stiffness position controller. We experimentally evaluated the following hypotheses by comparing our framework (M) with the baseline (B):

- **H1)** M achieves comparable or higher performance than B in the absence of a perturbation field, and outperforms B when the user has to interact with perturbations;
- **H2)** Regulation of joint stiffness and damping makes the interaction with the external perturbation more predictable: it is an effective strategy to adapt to perturbations;
- **H3)** M enables the user to better understand the properties of the perturbation field.

Evaluation procedure M and B were tested on separate days to avoid muscle tiredness and involuntary bias based on the order of training/evaluation. At the beginning of the experiment, the subject was told that different motor control strategies can be explored, e.g., relaxed movement and changing muscle co-activation, but the subject had no prior knowledge of M or B.

There were three stages in the evaluation process. In **stage 1** we analysed the task execution outcome based on six performance measures [32]: (i) *Success Rate (SR) [%]*: proportion of successful trials, with a trial considered successful if the subject reached the target and held the position for three seconds (max 20 secs); (ii) *Time to Reach (TR) [sec]*: time to complete the trial, with 20secs as the maximum time allowed; (iii) *Throughput (TP) [bit/sec]*: index of difficulty (ID) divided by TR to quantify the information conveyed during TR, with distance to target and size of target being factors of interest; (iv) *Path Efficiency (PE)*: the ratio between the length of the optimal path to target (Euclidean distance) and the length of the trajectory followed by the subject; (v) *Energy [J]*: time integral (over trial duration: $t_f - t_i$) of joint torque multiplied by joint velocity $\int_{t_i}^{t_f} \tau_f(t) \dot{q}_f dt$; and (vi) *Near Miss (NM) [#]*: number of times the subject entered the target circle, but did not maintain the position for three secs. In **stage 2**, we analysed task execution to better understand the control performance. We computed the *smoothness* of q_f using the SPARC measure [33] and the *Mutual Information (MI)* between the torque output of impedance controller τ_f and the simulated wrist position q_f . One-tailed Mann–Whitney U test was used (with all measures above) to measure the statistical significance (p-values < 0.05) of differences in performance. **Stage 3** explored the user's *perceived controllability* of our framework. Subjects were asked to answer six questions about M and B at the end of each experimental session: (i) Does your motor intent match cursor motion? (ii) Was your motor command executed in a timely manner? (iii) Was control precise or were there oscillations around the desired position? (iv) Describe the force field; (v) What was your strategy to counter perturbations? and (vi) Did impedance modulation help counter perturbations? The answer choices for the first three questions were: mostly good, good (with some instances of low controllability), and poor; the other three questions allowed free-form answers.

4.2 Experimental Results

We discuss some key insights here; additional results that aim to provide further insight into the muscle-tendon models and impedance adaptation are included as appendix sections to this document (Sections A.3, A.4, A.5).

The SR was 95% and 82.19% for M and B (respectively) without any perturbation, and 93.75% and 76.87% with the perturbation, i.e., unlike B, M consistently enabled successful task completion with or without perturbation. Figure 3 shows the values of some performance measures for the eight subjects; each point is the average over 40 trials for a subject. We observe that while M and B provide comparable values of TR and TP without any perturbation, M provides a significant improvement in TP with the perturbation. Also, M has a significantly higher PE than B with the perturbation; this is also reflected in the much lower values of NM (with/without perturbation) provided by M. Next, we observed that SPARC is significantly better with M compared with B, with or without perturbation. Similarly, we observe that M provides a significantly higher MI (between τ_f and q_f) than B with and without perturbation. Since M allows the subject to modulate joint stiffness and damping (and hence output torque), if the subject provides low torque, the simulated robot is more affected by any perturbation; this explains the observed outliers in TR and Energy, and the high(er) variance in SPARC, with M. B (on the other hand) uses a fixed high stiffness, which results in poor performance and high variance, particularly with perturbation. Furthermore, since subjects do not have any prior knowledge of M or B, some outliers may be due to the subject taking more time to understand how to successfully reach the target under different environmental conditions. Overall, these results strongly support hypotheses **H1** and **H2**.

Figure 4 summarizes user responses to Q1-3. Although we did not receive usable responses from some subjects for some questions, subjects indicated that M provided a better match between motor

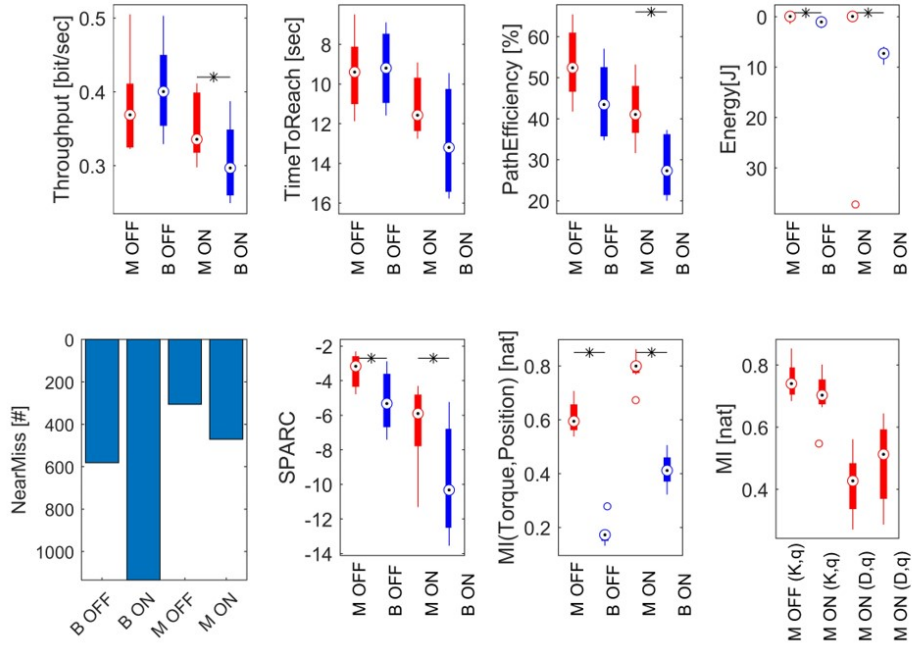


Figure 3: Values of performance measures: each group contains eight points (averaged over 40 trials for each subject). A statistically significant improvement of the median, computed between M OFF-B OFF and M ON-B ON, is highlighted with an asterisk.

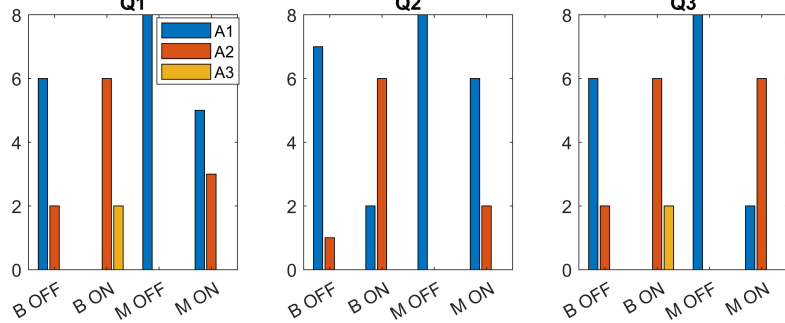


Figure 4: User responses to Q1-3 of the questionnaire, with and without external perturbations.

intent and cursor motion, resulting in more timely execution of the motor commands, and more precise control than B; these results were more pronounced in the presence of perturbations. For Q4, six out of eight subjects gave a correct description of the perturbation field when using M; with B, they could not correctly describe where the force field was localised. For Q5, all the subjects had the same control strategy with B: stay relaxed (low muscle co-contraction) and move the wrist until the joint limit is reached. With M, two subjects did not have to significantly increase muscle co-contraction, but the remaining six adapted the joint impedance to counter the perturbation. For Q6, all subjects agreed impedance modulation did not improve performance with B; two subjects stated that it resulted in the worst perceived controllability. With M, on the other hand, almost all subjects indicated that impedance adaptation helped counter the perturbation. These results support H3.

5 Conclusions, Limitations and Future Work

In this paper, we described a novel framework for a human-machine interface (HMI) that can be used to control an upper-limb prosthesis. The framework estimates a human's motor intent from noisy sEMG signals and executes this intent on a simulated robot arm. Our framework incorporates muscle-tendon models for each degree of freedom, with simultaneous online control of joint trajec-

tory, and modulation of stiffness and damping. In addition, it includes a method for learning model parameters to estimate motor intent and a variable impedance controller that automatically adapts gains and motion trajectory to complete the desired tasks even in the presence of previously unknown external perturbations. In the context of able-bodied humans using our HMI with a simulated robot arm to perform reaching tasks requiring actuation of a DoF in the wrist, we demonstrated a significant improvement in performance, and a better understanding of the robot’s operation, in comparison with a state of the art data-driven baseline. The framework reported in this paper presents promising insights and opens up multiple directions for further research. Specifically, we will conduct experiments with additional human subjects and thoroughly explore the impact of different representational choices in the muscle-tendon models. We also aim to explore the relative contribution of stiffness and damping to account for the perturbations; we will do so by designing experiments that involve reaching tasks in velocity-dependent force fields. Another interesting direction for future research is to explore simultaneous control of multiple DoFs. Furthermore, we will evaluate our framework on upper-limb amputees using a physical prosthesis.

A Appendix

In this section we provide:

- A.1** An example of trajectory tracking results obtained through an offline evaluation of the proposed framework (M) and a state-of-the-art data-driven baseline (B);
- A.2** The list of the muscle-tendon model parameters to be optimized and the constraints added to the optimization problem based on prior knowledge of the problem;
- A.3** The time evolution of the values of muscle-tendon space variables and joint space variables during a successful trial and during a failed trial for the reaching task with perturbation;
- A.4** The time evolution of joint space variables for the baseline during a failed trial (with perturbation), and two successful trials (one each with and without perturbation); and
- A.5** Additional results supporting the claims made in the main paper.

Recall that the proposed framework includes muscle-tendon models for each degree of freedom and a variable impedance controller for estimating human action intent from EMG signals and for adaptive, online execution of the intent in the presence of perturbations. The baseline, on the other hand, uses a neural network to directly map EMG signals to a trajectory that is passed through a fixed (high stiffness) PD controller for execution.

A.1 Offline training results example

We first describe the trajectory tracking results obtained through offline training and evaluation of the proposed framework (M) and the baseline (B) for a representative subject. We record the EMG signals as a human participant executes a given motion pattern through the simulated interface; this motion primarily focuses on the flexion-extension DoF. We also record the corresponding ground truth pose using an external high-fidelity motion capture system. Part of the recorded data is used to learn the values of the framework’s parameters; please see Figure 2 in the main paper. The trained framework (M or B) is then evaluated on the entire dataset, with the results summarized in Figures 5 and 6. In these figures, the black dotted line represents the ground truth trajectory of flexion-extension DoF. We observe that B achieves a lower tracking error (RMSE), but overestimates the repetitions performed at high impedance, e.g., between 80-150 secs in Figure 6. During data collection, the subject performs ulnar-radial deviation motions of the wrist (DoF 1) from $t = 275$ seconds. We observe some indirect activation of the DoF 2 (flexion-extension) during this interval because the two DoFs can not be completely decoupled. These indirect flexion-extension motions are overestimated by M (in Figure 5), potentially M trains separate muscle models based on specific EMG activations, whereas B jointly considers all eight EMG signals as inputs. However, B provides a more noisy estimate in Figure 6; it substantially over/under-estimates the trajectory in certain segments. Figure 6 only shows q_f because the use of a high (fixed) stiffness PD controller makes q_f very similar to the q_r produced by the neural network model.

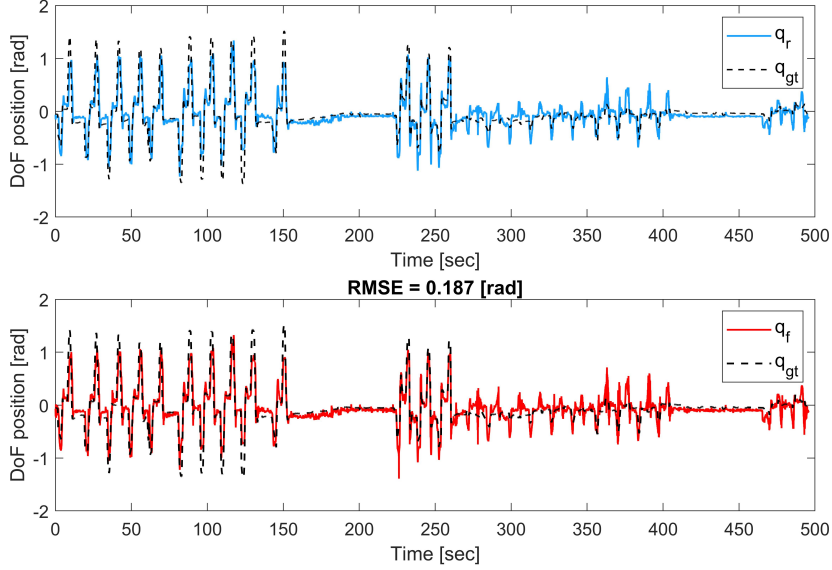


Figure 5: Trajectory tracking results during the off-line evaluation of the **proposed framework (M)**. The black dotted line is the ground truth position (q_{gt}) of the flexion-extension DoF. The reference trajectory computed from the output of the muscle-tendon model is in blue (q_r), while the overall trajectory after the variable impedance controller is in red (q_f).

A.2 Muscle-tendon parameter space

Table 1 lists the muscle-tendon parameters \bar{p}^i of MTU_i . The values of these parameters are learned through an optimization process (close to the end of Section 3 of the main paper). Additionally, the main constraints of the optimization task are listed below:

- $W_{des}^i + W_{asc}^i < l_{ceInit}^i$, where l_{ceInit}^i is the initial state of the muscle when $q_r = 0$
- if $l_{ce}^i < 0.001l_{opt}^i$ or $l_{ce}^i > 0.95(l_{MTU}^i - l_{see0}^i)$ set $\dot{l}_{ce}^i = 0$
- constraints on joint stiffness and damping $K > 0, D \geq 0$

Other constraints to the parameter space are defined numerically as upper/lower bounds on the values of these parameters; these are set experimentally based on prior work [29]. For more details about the muscle-tendon structure and contraction dynamics, please see [23].

A.3 State evolution in proposed framework during reaching tasks

We show plots corresponding to two illustrative examples of reaching tasks in the presence of a perturbation field. In the first example shown in Figure 7, the subject successfully reaches the target, whereas the second example shown in Figure 8 corresponds to a failed trial. In each figure, we plot the following signals:

- A normalised input to the muscle-tendon models (ch_4, ch_8) representative of the activity of the flexor and extensor muscles.
- B joint position q_r (dotted green line) output by forward dynamics and q_f (continuous green line) output by the impedance controller, as the subject attempts to move q_f from the initial position (black dotted line) to the target position (continuous black line).
- C forces generated by the muscle-tendon elements of MTU_1 .
- D forces generated by the muscle-tendon elements of MTU_2 .
- E stiffness of $muscle_1$ (K_1^M) and $muscle_2$ (K_2^M), and the stiffness of $tendon_1$ (K_1^T) and $tendon_2$ (K_2^T).
- F damping of $muscle_1$ (K_1^M) and $muscle_2$ (K_2^M), and the damping of $tendon_1$ (K_1^T) and $tendon_2$ (K_2^T).

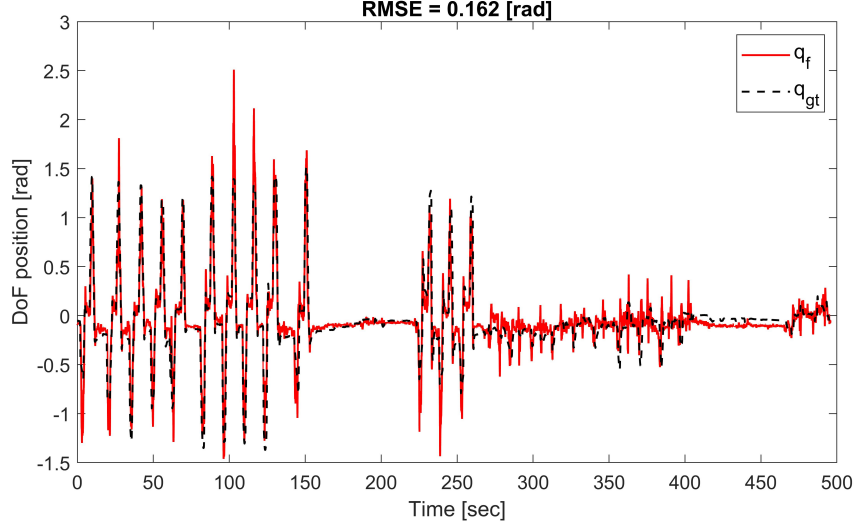


Figure 6: Trajectory tracking results during off-line evaluation of the **baseline (B)**. The black dotted line is the ground truth position (q_{gt}) of the flexion-extension DoF, while the output of B after using the trained neural network model and fixed PD controller (q_f) is indicated in red. We report the RMSE between q_f and q_{gt} .

	Parameter Name	Parameter Description	Variable	Lower Bound	Upper Bound
CE	F_{max}	Maximum isometric force F_{iso}	\bar{p}_1	1000	6000
	l_{opt}	Shortest l_{ce} / $F_{ce} = F_{max}$	$\bar{p}_2 l_{ce}^{init}$	$0.05l_{ce}^{init}$	$0.085l_{ce}^{init}$
	W_{des}	Width of normalised descending branch of F_{iso}	$\bar{p}_3 \bar{p}_2$	$0.7\bar{p}_2$	$3.5\bar{p}_2$
	W_{asc}	Width of normalised ascending branch of F_{iso}	$\bar{p}_4 \bar{p}_2$	$0.7\bar{p}_2$	$3.5\bar{p}_2$
	v_{des}	exponent of descending branch of F_{iso}	\bar{p}_5	1.2	3
	v_{asc}	exponent of ascending branch of F_{iso}	\bar{p}_6	1.2	3
	A_{max}	max value of Arel	\bar{p}_7	0.1	0.4
	B_{max}	max value of Brel	\bar{p}_8	1.1	5.1
PEE	l_{pee0}	rest length of PEE	$\bar{p}_9 \bar{p}_2$	$0.7\bar{p}_2$	$0.95\bar{p}_2$
	v_{pee}	exponent of PEE force	\bar{p}_{10}	1.1	3
	f_{pee0}	force of PEE if l_{ce} is stretched to ΔW_{des}	$\bar{p}_{11} \bar{p}_1$	$0.5\bar{p}_1$	$1\bar{p}_1$
DE	D	dimensionless factor to scale d_{SE}^{max}	\bar{p}_{12}	0.001	3
	R	minimum value of d_{SE} normalised to d_{SEmax}	\bar{p}_{13}	0	0.8
SEE	l_{see0}	tendon slack length	$\frac{2}{3}l_{MTU}$	-	-
	ΔU_{nl}	relative stretch at non-linear linear transition	\bar{p}_{14}	0.02	0.07
	ΔU_l	relative stretch in the linear part providing a force increase of ΔF_{see0}	$\bar{p}_{14} \bar{p}_{15}$	$(1/3)\bar{p}_{15}$	$(2/3)\bar{p}_{15}$
	ΔF_{see0}	force at the transition from non-lin to lin area, and force increase in the linear part	$\bar{p}_{16} \bar{p}_1$	$0.3\bar{p}_1$	$1\bar{p}_1$
	S	relation between F(v) slopes at $\bar{l}_{ce} = 0$	\bar{p}_{17}	1.2	2
	F	factor by which the force can exceed F_{max} for large eccentric velocities	\bar{p}_{18}	0.5	2

Table 1: The main parameters that define the structure of each muscle-tendon unit. The last column shows the variables to be optimized for the corresponding parameter.

G stiffness of the muscle-tendon units in the joint space (black signal), where the red signal is the stiffness contribution of the contraction dynamics of the muscle-tendon units and the blue signal is the stiffness contribution of the moment arms as a function of $q_r(t)$.

H the damping of the muscle-tendon units in the joint space.

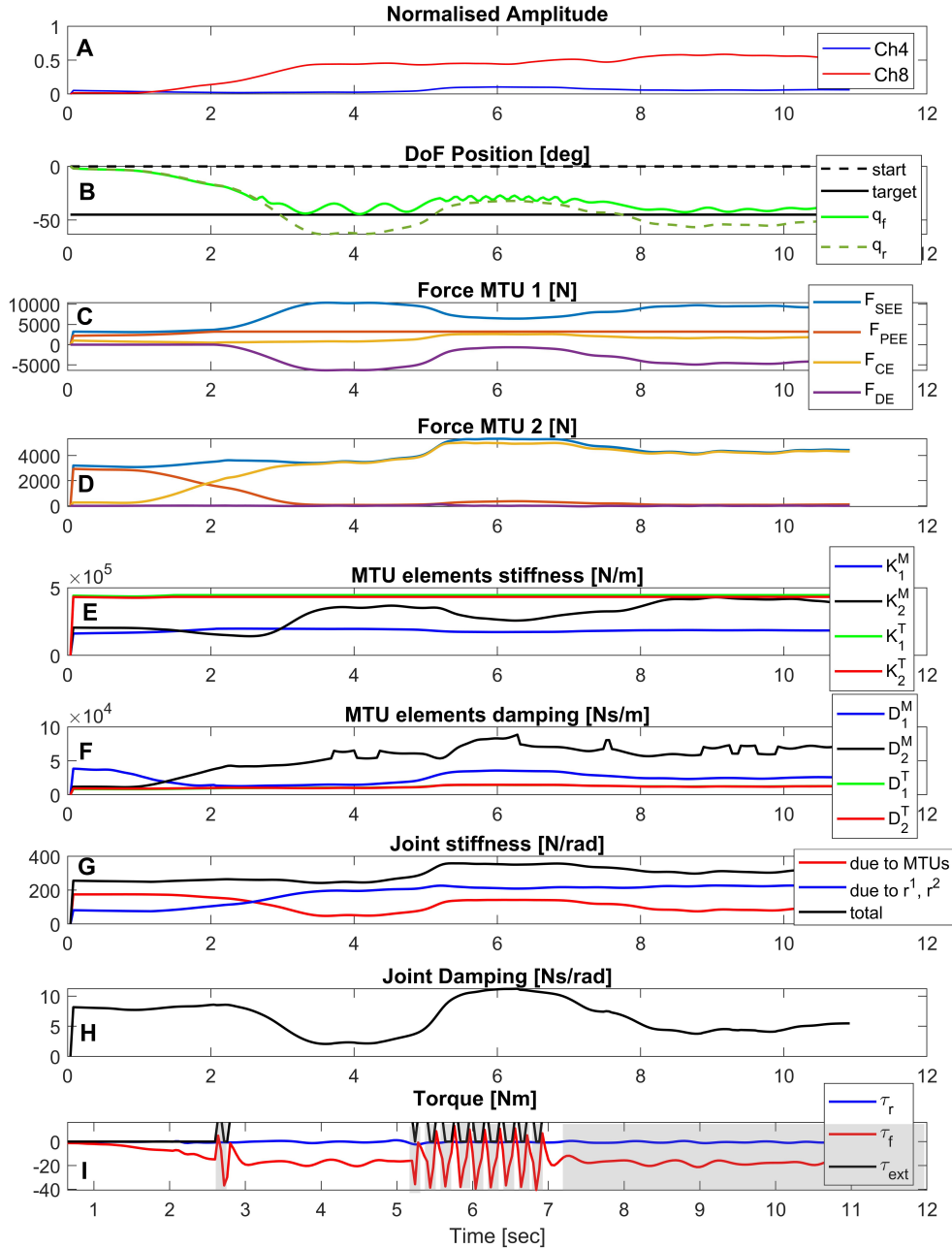


Figure 7: **Proposed method (M).** Example of a successful trial. We plot the time evolution of the most relevant muscle-tendon variables and controller/robot variables while the subject performs a reaching task in the presence of a perturbation field. The system stabilises in less than two seconds.

I the torque command provided by the impedance controller τ_f and the perturbation torque τ_{ext} due to the force field.

In the first example, the subject receives visual feedback on the effect of the perturbation and modifies their muscle activation in an attempt to negate the effect of the perturbation; the increase in co-activation in Figure 7-A during the time interval of 5-8 seconds corresponds to an increase in joint stiffness K_2^M and damping D_2^M (see Figure 7-G, H). In Figure 7-B, we observe a discrepancy between q_r , unaffected by the perturbation field, and q_f , the output of the position-based impedance controller which "tracks" q_r using the joint stiffness and damping based on the estimates provided

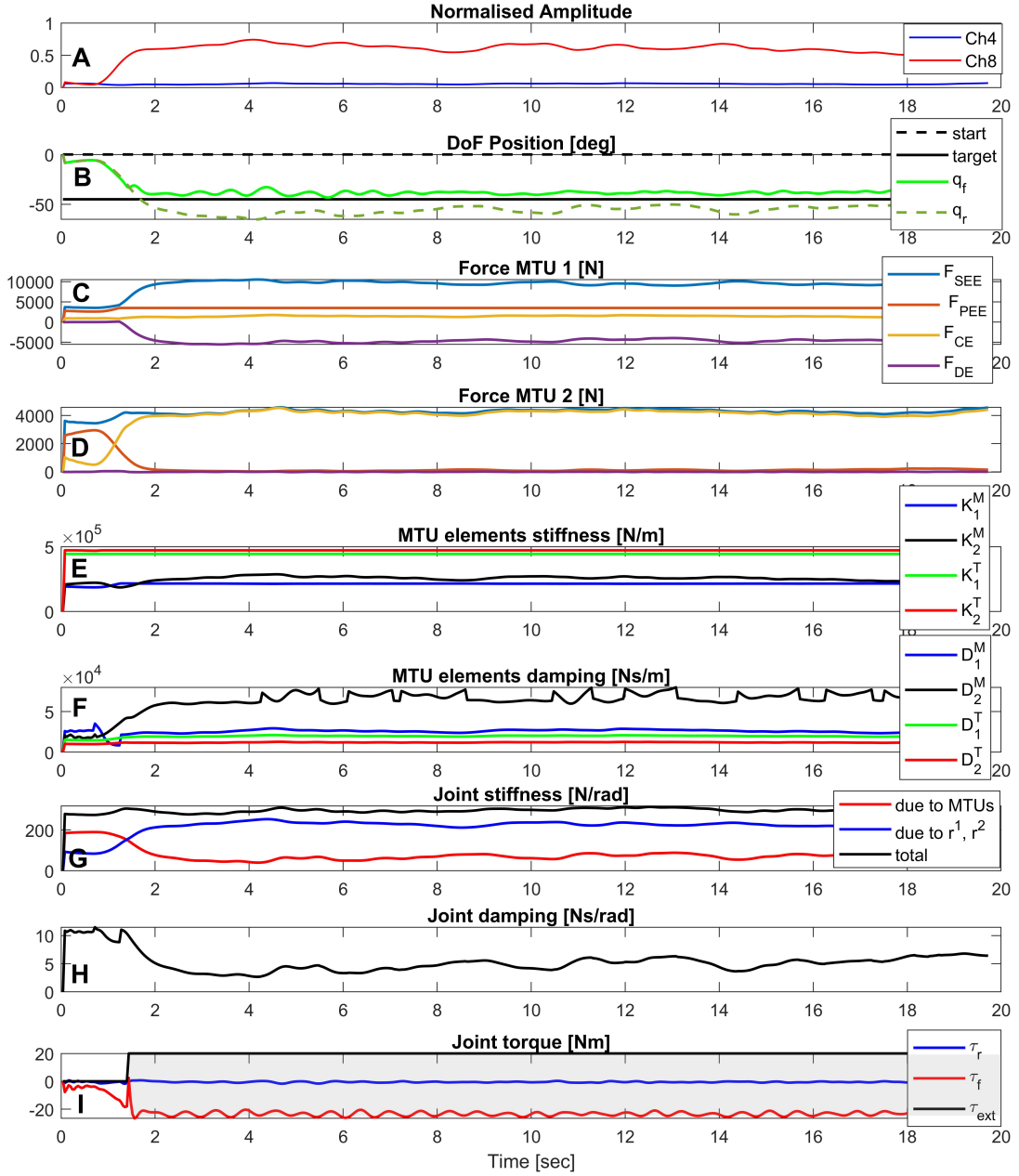


Figure 8: **Proposed method (M).** Example of failed trial. We plot the time evolution of the most relevant muscle-tendon variables and controller/robot variables while the subject performs a reaching task in the presence of a perturbation field.

by the muscle-tendon models. The error between the two trajectories decreases when the subject modulates the wrist impedance.

The time intervals during which the subject experiences the perturbation field is shaded gray in Figure 7-I and τ_{ext} is not equal to zero. Figure 7-D shows the forces generated by the elements of MTU_2 , the muscle-tendon unit corresponding to flexion, i.e., contracting the muscle. We observe that the force generated by the active element and by the elastic component of the tendon, F_{CE} and F_{SEE} respectively, are mainly active. In the second example, on the other hand, only the (agonist) muscle-tendon unit MTU_2 is being activated. We thus hypothesise that the low co-activation has an

impact on task performance and the ability to counter the perturbation, as the subject cannot generate the necessary torque to move through the perturbation field.

A.4 State evolution in baseline framework during reaching task

We show plots corresponding to three illustrative examples of reaching tasks with the baseline framework: Figure 9 depicts a failed trial perturbation; Figure 10 depicts a successful trial in which the subject counters the effect of the perturbation field; and Figure 11 summarizes a successful trial in the absence of perturbations. In each figure, we plot the following signals:

- A** normalised EMG channels (ch_4, ch_8) representative of the activity of the flexor and extensor muscles. Recall that the baseline algorithm considers all eight EMG signals from the myoband as input;
- B** joint position q_r (dotted green line) output by the neural network, q_f (continuous green line) output by the PD controller when tracking q_r , as the subject attempts to move q_f from the initial position (black dotted line) to the target position (continuous black line);
- C** joint velocity;
- D** torque output provided by the PD controller (τ_f) and the perturbation torque due to the force field (τ_{ext}).

We observe that although the magnitude of ch_8 in Figure 9-A is approximately five times the magnitude of ch_8 in Figure 10-A, the reference joint position q_r output by the neural network estimator is (on average) very similar. The difference is in the smoothness of the estimated trajectory; it is less smooth in Figure 9-B, potentially due to the higher co-activation of the muscles. This may be the reason why the first trial resulted in a failure whereas the second one was successful. This experimental result, and our (potential) explanation of how co-contraction of muscles results in successful trials, reflect the feedback provided by the human subjects regarding their strategy to counter perturbations when using B (see the last paragraph of Section 4 of the main paper).

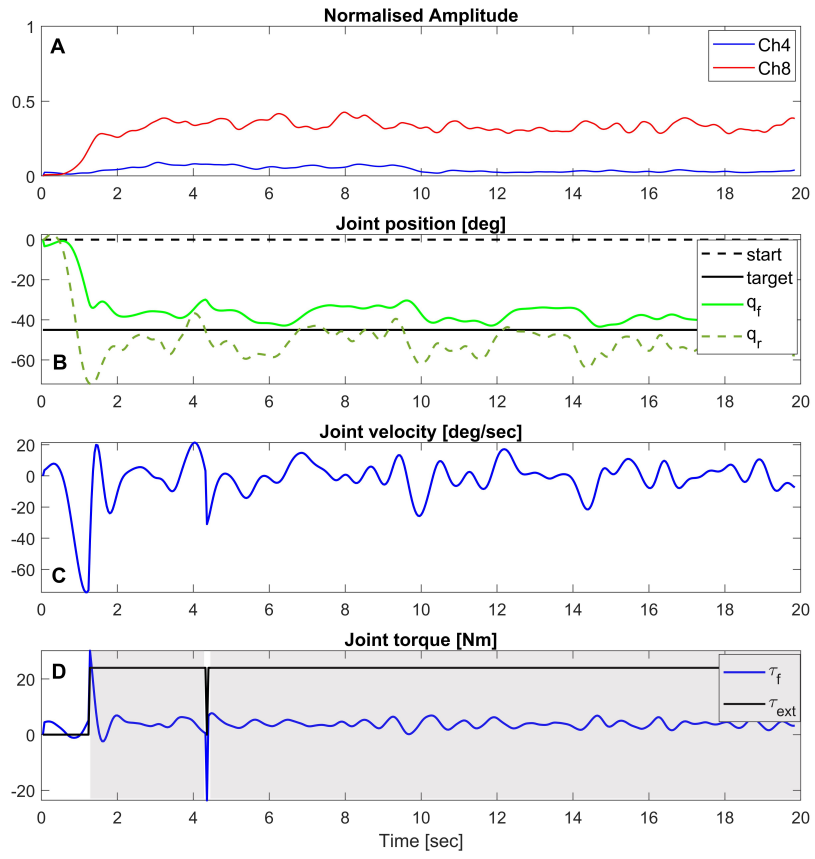


Figure 9: **Proposed method B.** Here we plot the time evolution of the controller/robot variables, while the subject performs a reaching task in the presence of a perturbation field. The subject fails to stabilize the system and passes through the force field.

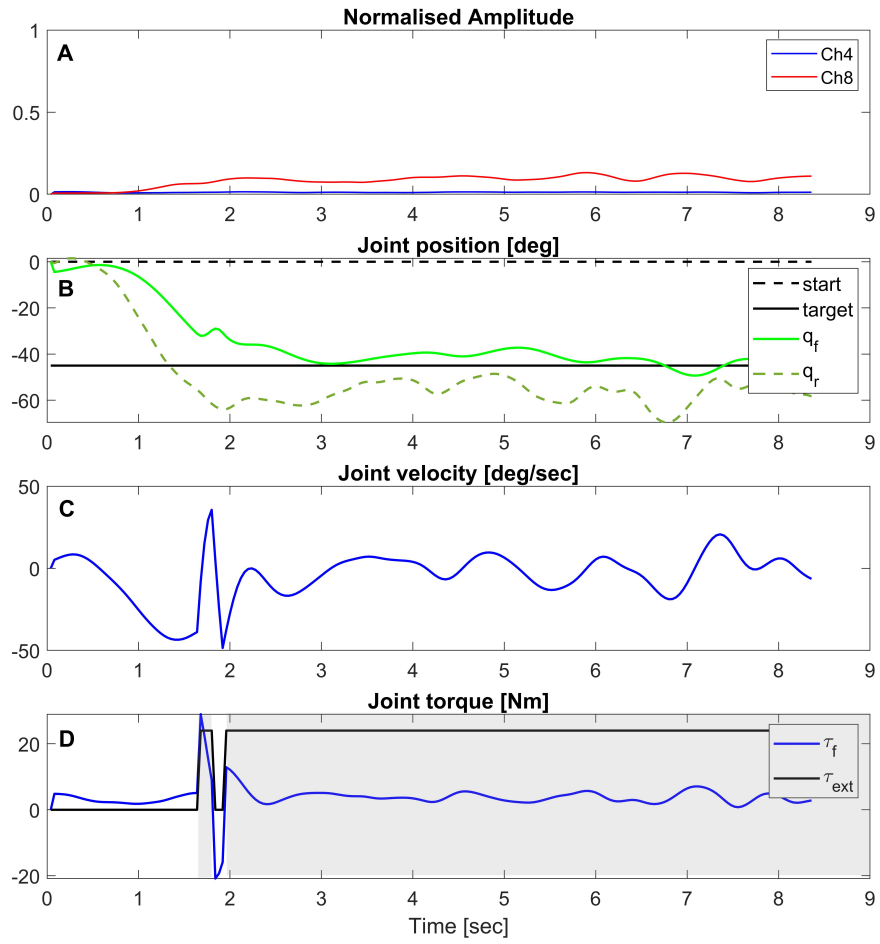


Figure 10: **Proposed method B.** Here we plot the time evolution of the controller/robot variables, while the subject performs a reaching task in the presence of a perturbation field. Example of successful trial where the subject is able to counter the perturbation field

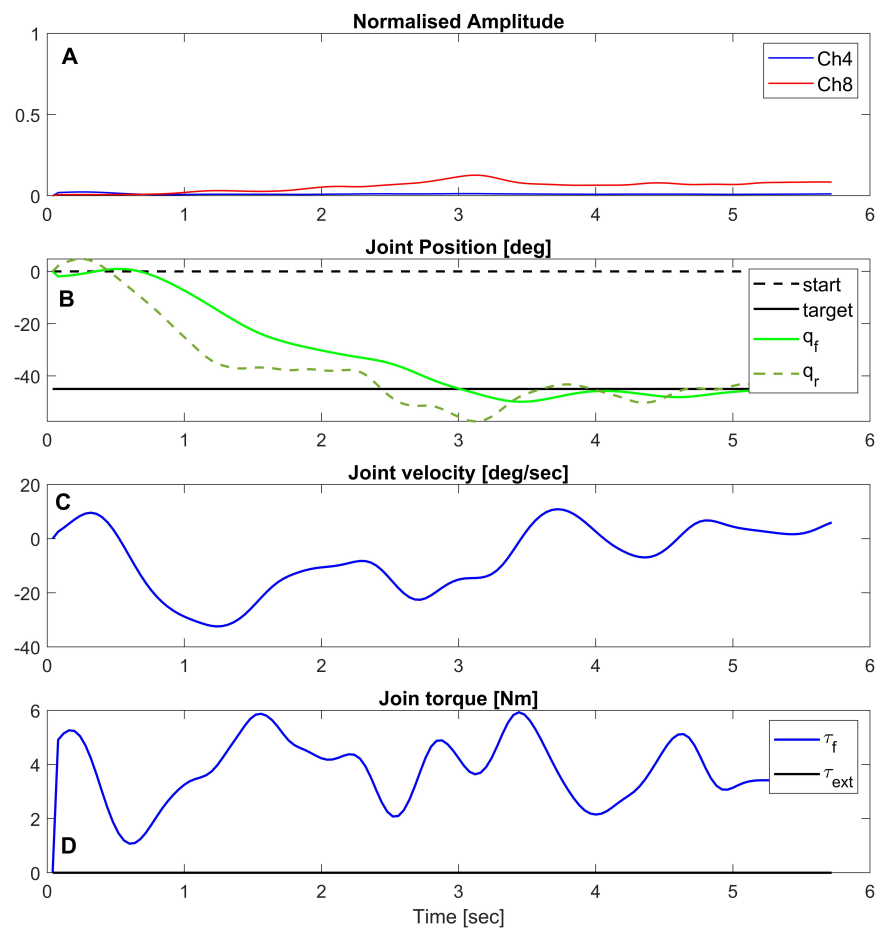


Figure 11: **Proposed method B.** Here we plot the time evolution of the controller/robot variables, while the subject perform a reaching task in the absence of a perturbation field.

A.5 Additional experimental results

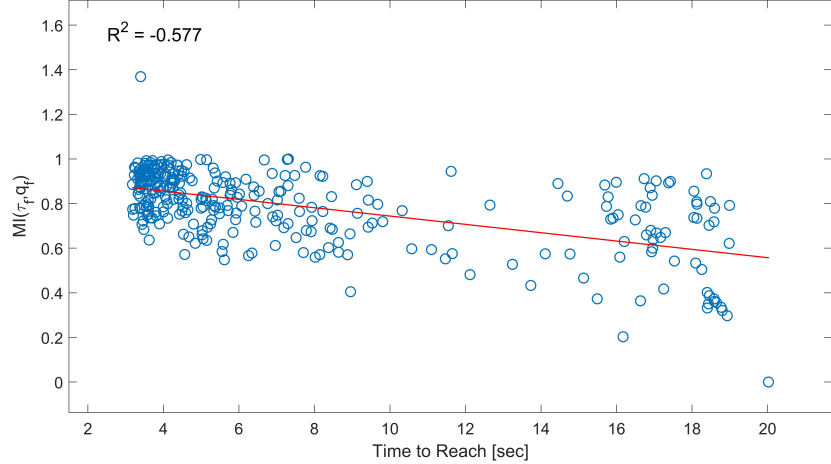


Figure 12: **Proposed framework.** Scatter plot of the mutual information between τ_f (from impedance controller) and q_f , and the time to reach metric.

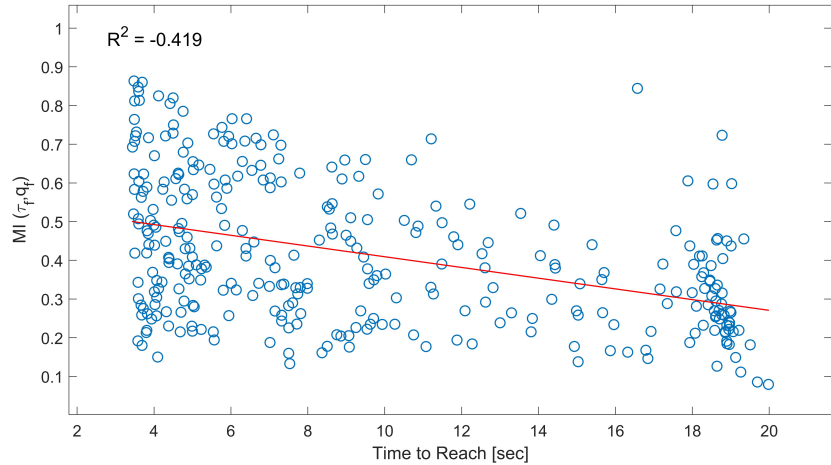


Figure 13: **Baseline.** Scatter plot of the mutual information between τ_f (from PD controller) and q_f , and the time to reach metric.

Finally, we explored the relationship between the mutual information (between τ_f and q_f) and the Time to Reach metric, for both M and B as shown in Figure 12 and Figure 13 respectively. We notice that the experimental trials with a low "time to reach" have high mutual information for M, while there is no such correlation for B.

Acknowledgments

This work was supported in part by a studentship from the *Physical Sciences for Health* Centre for Doctoral Training funded by the UK Engineering and Physical Sciences Research Council (EP/L016346/1). The authors thank Dr. Deren Barsakcioglu, Dr. Moon Ki Jung, Irene Mendez Guerra and Milia Helena Hasbani for technical support with the use of EMGs, and thank Dr. Morteza Azad for his co-supervision at the beginning of the project.

References

- [1] J. M. Hahne, M. Markovic, and D. Farina. User adaptation in myoelectric man-machine interfaces. *Scientific reports*, 7(1):1–10, 2017.
- [2] S. Muceli and D. Farina. Simultaneous and proportional estimation of hand kinematics from EMG during mirrored movements at multiple degrees-of-freedom. *IEEE Transactions on Neural Systems and Rehabilitation Engineering*, 20(3):371–378, 2012.
- [3] N. Jiang, I. Vujaklija, H. Rehbaum, B. Graimann, and D. Farina. Is accurate mapping of emg signals on kinematics needed for precise online myoelectric control? *IEEE Transactions on Neural Systems and Rehabilitation Engineering*, 22(3):549–558, 2013.
- [4] P. Capsi-Morales, C. Piazza, M. G. Catalano, A. Bicchi, and G. Grioli. Exploring stiffness modulation in prosthetic hands and its perceived function in manipulation and social interaction. *Frontiers in Neurorobotics*, page 33, 2020.
- [5] E. Hocaoglu and V. Patoglu. sEMG-based natural control interface for a variable stiffness transradial hand prosthesis. *Frontiers in Neurorobotics*, 16, 2022.
- [6] N. Karavas, A. Ajoudani, N. Tsagarakis, J. Saglia, A. Bicchi, and D. Caldwell. Tele-impedance based assistive control for a compliant knee exoskeleton. *Robotics and Autonomous Systems*, 73:78–90, 2015.
- [7] C. M. Niu, Q. Luo, C.-h. Chou, J. Liu, M. Hao, and N. Lan. Neuromorphic model of reflex for realtime human-like compliant control of prosthetic hand. *Annals of Biomedical Engineering*, 49(2):673–688, 2021.
- [8] R. Osu, D. W. Franklin, H. Kato, H. Gomi, K. Domen, T. Yoshioka, and M. Kawato. Short- and long-term changes in joint co-contraction associated with motor learning as revealed from surface emg. *Journal of neurophysiology*, 88(2):991–1004, 2002.
- [9] N. Hogan. The mechanics of multi-joint posture and movement control. *Biological cybernetics*, 52(5):315–331, 1985.
- [10] T. Flash and F. Mussa-Ivaldi. Human arm stiffness characteristics during the maintenance of posture. *Experimental brain research*, 82(2):315–326, 1990.
- [11] E. J. Perreault, R. F. Kirsch, and P. E. Crago. Effects of voluntary force generation on the elastic components of endpoint stiffness. *Experimental brain research*, 141(3):312–323, 2001.
- [12] N. Hogan. Impedance control: An approach to manipulation: Part ii—implementation. 1985.
- [13] A. Furui, S. Eto, K. Nakagaki, K. Shimada, G. Nakamura, A. Masuda, T. Chin, and T. Tsuji. A myoelectric prosthetic hand with muscle synergy-based motion determination and impedance model-based biomimetic control. *Science Robotics*, 4(31):eaaw6339, 2019.
- [14] T. Tsuji, K. Shima, N. Bu, and O. Fukuda. Biomimetic impedance control of an em-based robotic hand. *Robot Manipulators: Trends and Development*, page 213, 2010.
- [15] J. M. Hahne, F. Biessmann, N. Jiang, H. Rehbaum, D. Farina, F. Meinecke, K.-R. Müller, and L. Parra. Linear and nonlinear regression techniques for simultaneous and proportional myoelectric control. *IEEE Transactions on Neural Systems and Rehabilitation Engineering*, 22(2):269–279, 2014.
- [16] L. H. Smith, T. A. Kuiken, and L. J. Hargrove. Evaluation of linear regression simultaneous myoelectric control using intramuscular emg. *IEEE Transactions on Biomedical Engineering*, 63(4):737–746, 2015.
- [17] D. Yeung, I. M. Guerra, I. Barner-Rasmussen, E. Siponen, D. Farina, and I. Vujaklija. Co-adaptive control of bionic limbs via unsupervised adaptation of muscle synergies. *IEEE Transactions on Biomedical Engineering*, 2022.

- [18] A. Krasoulis, S. Vijayakumar, and K. Nazarpour. Evaluation of regression methods for the continuous decoding of finger movement from surface emg and accelerometry. In *2015 7th International IEEE/EMBS Conference on Neural Engineering (NER)*, pages 631–634. IEEE, 2015.
- [19] P. Xia, J. Hu, and Y. Peng. Emg-based estimation of limb movement using deep learning with recurrent convolutional neural networks. *Artificial organs*, 42(5):E67–E77, 2018.
- [20] I. Vujaklija, V. Shalchyan, E. N. Kamavuako, N. Jiang, H. R. Marateb, and D. Farina. Online mapping of emg signals into kinematics by autoencoding. *Journal of neuroengineering and rehabilitation*, 15(1):1–9, 2018.
- [21] A. V. Hill. The heat of shortening and the dynamic constants of muscle. *Proceedings of the Royal Society of London. Series B-Biological Sciences*, 126(843):136–195, 1938.
- [22] T. S. Buchanan, D. G. Lloyd, K. Manal, and T. F. Besier. Neuromusculoskeletal modeling: estimation of muscle forces and joint moments and movements from measurements of neural command. *Journal of applied biomechanics*, 20(4):367, 2004.
- [23] M. Günther, S. Schmitt, and V. Wank. High-frequency oscillations as a consequence of neglected serial damping in hill-type muscle models. *Biological cybernetics*, 97(1):63–79, 2007.
- [24] M. Sartori, M. Reggiani, D. Farina, and D. G. Lloyd. Emg-driven forward-dynamic estimation of muscle force and joint moment about multiple degrees of freedom in the human lower extremity. *PloS one*, 7(12):e52618, 2012.
- [25] N. Hogan. Mechanical impedance of single-and multi-articular systems. In *Multiple muscle systems*, pages 149–164. Springer, 1990.
- [26] J. M. Winters. Hill-based muscle models: a systems engineering perspective. In *Multiple muscle systems*, pages 69–93. Springer, 1990.
- [27] M. Bennett1, R. Ker1, N. J. Imery, and R. M. Alexander1. Mechanical properties of various mammalian tendons. *Journal of Zoology*, 209(4):537–548, 1986.
- [28] D. G. Lloyd and T. F. Besier. An emg-driven musculoskeletal model to estimate muscle forces and knee joint moments in vivo. *Journal of biomechanics*, 36(6):765–776, 2003.
- [29] C. Y. Scovil and J. L. Ronsky. Sensitivity of a hill-based muscle model to perturbations in model parameters. *Journal of biomechanics*, 39(11):2055–2063, 2006.
- [30] P. J. Van Laarhoven and E. H. Aarts. Simulated annealing. In *Simulated annealing: Theory and applications*, pages 7–15. Springer, 1987.
- [31] K. Kronander and A. Billard. Learning compliant manipulation through kinesthetic and tactile human-robot interaction. *IEEE transactions on haptics*, 7(3):367–380, 2013.
- [32] M. R. Williams and R. F. Kirsch. Evaluation of head orientation and neck muscle emg signals as command inputs to a human–computer interface for individuals with high tetraplegia. *IEEE Transactions on Neural Systems and Rehabilitation Engineering*, 16(5):485–496, 2008.
- [33] S. Balasubramanian, A. Melendez-Calderon, A. Roby-Brami, and E. Burdet. On the analysis of movement smoothness. *Journal of neuroengineering and rehabilitation*, 12(1):1–11, 2015.